International Journal of Heat and Mass Transfer 52 (2009) 4535–4544

Contents lists available at ScienceDirect

International Journal of Heat and Mass Transfer

journal homepage: www.elsevier.com/locate/ijhmt

Tree-shaped vascular wall designs for localized intense cooling

L.A.O. Rocha [a], S. Lorente [b], A. Bejan [c,*]

[a] Federal University of Rio Grande, School of Engineering, Av. Itália km 8, Cx. P. 474, Rio Grande, RS 96.201-900, Brazil
[b] Université de Toulouse, INSA, Laboratoire Matériaux et Durabilité des Constructions, 135, Avenue de Rangueil, F-31077 Toulouse Cedex 04, France
[c] Duke University, Department of Mechanical Engineering and Materials Science, Box 90300, Durham, NC 27708-0300, USA

ARTICLE INFO

Article history:
Received 20 January 2009
Received in revised form 12 March 2009
Accepted 12 March 2009
Available online 7 May 2009

Keywords:
Constructal
Tree networks
Vascularization
Self-cooling
Smart materials
Fire wall design

ABSTRACT

This paper is a proposal to embed tree-shaped vasculatures in a wall designed such that the wall withstands without excessive hot spots the intense heating that impinges on it. The vasculature is a quilt of square-shaped panels, each panel having a tree vasculature that connects the center with the perimeter. The coolant may flow in either direction, center–perimeter, or perimeter–center, although here only the center–perimeter flow direction is illustrated. Numerical simulations of conjugate heat and fluid flow in three directions show that it is possible to determine all the optimal geometric features of vasculatures with up to three levels of bifurcation ($n = 3$). The global performance is evaluated in terms of the overall thermal resistance, pressure difference, flow resistance and pumping power. The improvements in global performance diminish as the number of bifurcation levels increases. No flow architecture is universally superior. The dendritic designs are superior at the low and high ends of the pressure difference range. The radial designs are superior at intermediate pressure difference numbers.

1. Introduction

Constructal theory guides engineers toward the discovery of efficient flow architectures for fluid, mass, energy and movement in general. The emerging designs are validated by comparisons with nature, in animate and inanimate systems. The constructal law recognizes the tendency of all flow systems to seek and find configurations for greater access in time: "For a finite-size flow system to persist in time (to live), it must evolve in such a way that it provides easier access to the currents that flow through it" [1–6]. The constructal law is not about *what* flows – fluid, energy, momentum, goods, or people – but about *how* the flow system acquires its architecture.

For example, dendritic flow architectures are derived from the constructal law as flow structures that connect effectively one point (source, or sink) and an infinity of points (curve, area, or volume). In a constructal tree there are at least two flow modes. The slow mode means diffusion, seepage, and the all high-unit-cost processes such as walking and hand delivery. These flows are allocated to the interstices of the tree architecture. The fast mode resides in channels with high conductivity and high permeability, such as the streams of water and vehicular traffic. In the convection cooling of a vascularized wall under intense heating, the channels are occupied by the convecting fluid, and the interstices are the solid structure that conducts the heat to the flow channels. Interstices and channels are optimally allocated to each other, and the result – the tree – represents the balance between the resistance across interstices and the resistance along channels.

Tree-shaped architectures offer lower pumping power requirements and higher 'densities' of heat and mass transfer than conventional architectures with bundles of parallel channels, or stacks of identical elements [7–15]. Possible applications are fuel cells and electronics packaging, which is an essential technology in thermal control. At much larger scales, the same concept can be applied to the design of thermal protection of solid walls in burners used in metallurgy, power plants and distillation plants.

In this paper, we propose to use dendritic flow architectures as a "fire wall" concept (Fig. 1) for the thermal management of future high-performance vehicles. The current literature reviewed in Ref. [16] suggests that the switch from classical architectures to dendritic architectures represents the future of high-compactness technologies such as the cooling of electronics (avionics) and the aggregation of fuel cells into high-power units with minimum weight.

2. Numerical model

Consider first the three-dimensional structure shown in Fig. 2. The structure consists of a square slab $2L \times 2L$ with the thickness t. The slab is insulated except on the bottom surface where it receives the uniform heat flux q''. The body is cooled by fluid that flows through ducts of square cross-section ($D_0 \times D_0$), which are

* Corresponding author. Tel.: +1 919 660 5310; fax: +1 919 660 8963.
E-mail address: abejan@duke.edu (A. Bejan).

0017-9310/$ - see front matter © 2009 Elsevier Ltd. All rights reserved.
doi:10.1016/j.ijheatmasstransfer.2009.03.003

Nomenclature

Be	dimensionless pressure difference, Eq. (9)
c_P	specific heat at constant pressure (J kg^{-1} K^{-1})
$\widetilde{C}$	specific heat ratio, $c_{P,s}/c_{P,f}$
D	size of the square ducts (m)
k	thermal conductivity of fluid, (W m^{-1} K^{-1})
$\widetilde{k}$	thermal conductivity ratio, k_s/k_f
L	length (m)
$\widetilde{m}$	dimensionless mass flow rate
n	number of bifurcations
P	pressure (Pa)
Pr	Prandtl number, ν/α
q''	heat flux (W m^{-2})
t	thickness (m)
T	temperature (K)
V	velocity (m/s)
V_p	total volume occupied by ducts (m^3)
V_t	body volume (m^3)
x, y, z	coordinates (m)

Greek symbols

α	thermal diffusivity (m^2/s)
α, β, γ, δ	angles (°)
μ	viscosity (kg s^{-1} m^{-1})
ρ	density (kg m^{-3})
$\widetilde{\rho}$	density ratio, ρ_s/ρ_f
Φ	volume fraction, V_p/V_t

Subscripts

f	fluid
max	maximum
m	minimum
mm	minimized twice
mmm	minimized three times
o	optimal
oo	optimized twice
p	path
ref	reference
s	solid
t	total
tr	triangle

Superscripts

(∼)	dimensionless variables, Eqs. (9) and (10)

embedded in the slab. The ducts are dug into the top surface of the slab. They continue with 90° turns [see the position $(0, y_1, t)$] and lead to the bottom surface where they bifurcate on the way to the two outlets located in the corners of the bottom surface. The flow is driven by the pressure difference ΔP maintained between the inlet (the center of the square slab) and the outlets shown in Fig. 2.

The objective is to discover the flow structure that minimizes the hot-spot temperatures regardless of their location. Because of symmetry, consider only one-eighth of the body. There are two constraints to consider. One is the total volume of the slab

$$V_t = \left(\frac{1}{2}L^2 - A_{tr}\right)t \tag{1}$$

where A_{tr} is the area of the triangle which is the upper surface of the volume disregarded of the body

$$A_{tr} = \frac{D_0^2}{4\tan(\pi/8)} \tag{2}$$

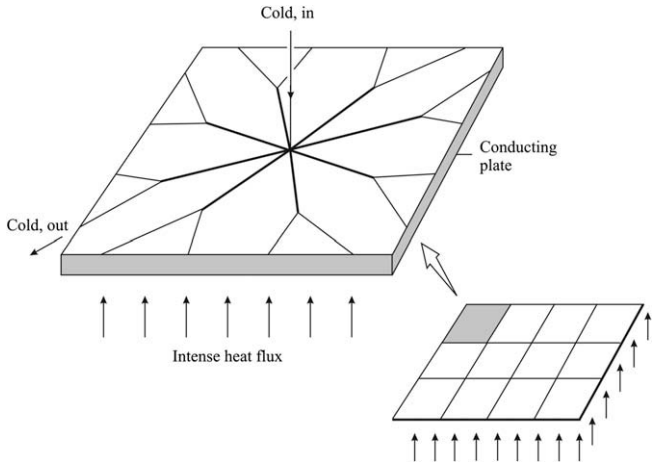

Fig. 1. Constructal 'fire wall' concept with embedded dendritic coolant architecture.

The other constraint is the volume occupied by the ducts,

$$V_p = \left(\frac{L}{\cos\alpha} + t + L - \frac{5}{2}D_0\right)D_0^2 \tag{3}$$

where the angle α is defined in Fig. 2. The V_p and V_t constraints can be combined to define the fixed volume fraction occupied by ducts,

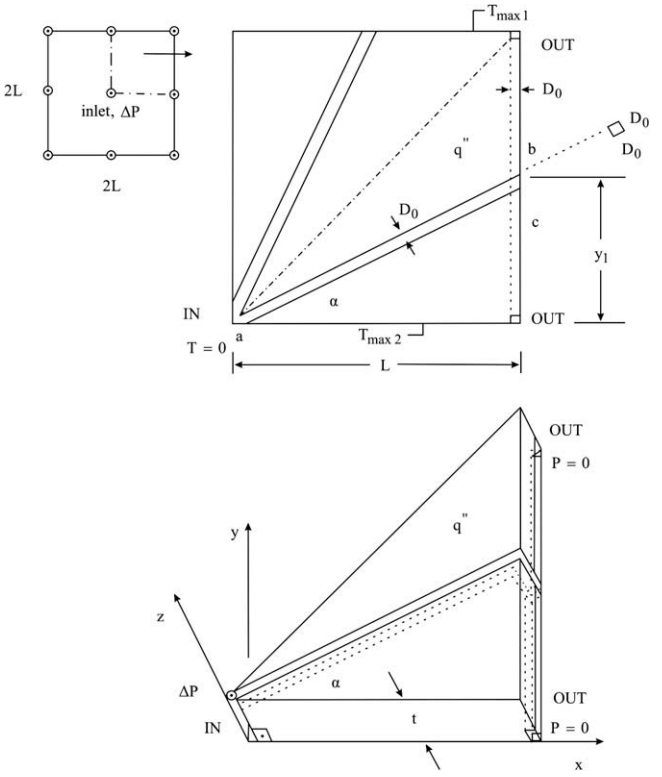

Fig. 2. Design with radial channels for cooling a square slab heated uniformly on its bottom side.

$$\phi = \frac{V_p}{V_t} \tag{4}$$

The structure of Fig. 2 was morphed and optimized numerically by simulating the three-dimensional temperature field in a large number of configurations obtained by varying the coordinates of point $b(0, y_1, t)$, or the angle α, and calculating the maximum temperature T_{max}. The search was for the configuration with minimum hot-spot temperature T_{max}. The flow was modeled as steady with constant properties, and laminar in three dimensions. The three-dimensional conservation equations are employed in the fluid region

$$\frac{\partial V_i}{\partial x_i} = 0 \tag{5}$$

$$\rho_f \left(\frac{\partial (V_i V_j)}{\partial x_i} \right) = \frac{\partial}{\partial x_i} \left(\mu \frac{\partial V_j}{\partial x_i} \right) - \frac{\partial P}{\partial x_i} \tag{6}$$

$$\rho_f \frac{\partial (V_i c_{p,f} T)}{\partial x_i} = \frac{\partial}{\partial x_i} \left(k_f \frac{\partial T}{\partial x_i} \right) \tag{7}$$

The equation for steady state conduction is used for the solid body

$$\frac{\partial}{\partial x_i} \left(\frac{\partial T}{\partial x_i} \right) = 0 \tag{8}$$

The results are presented in dimensionless form by using the dimensionless variables

$$\tilde{x}, \tilde{y}, \tilde{z}, \tilde{D}_0 = \frac{x, y, z, D_0}{L} \quad \tilde{T} = \frac{T - T_{min}}{q'' L / k_f} \quad Pr = \frac{\nu}{\alpha} \quad \mathrm{Be} = \frac{\Delta P L^2}{\mu \alpha} \tag{9}$$

$$\tilde{P} = \frac{P - P_{ref}}{\Delta P} \quad \frac{k_s}{k_f} = \tilde{k} \quad \frac{c_{p,s}}{c_{p,f}} = \tilde{C} \quad \frac{\rho_s}{\rho_f} = \tilde{\rho} \tag{10}$$

where P_{ref} is the pressure at the outlets, T_{min} is the fluid inlet temperature, k_f is the thermal conductivity of the fluid and μ is the viscosity. The dimensionless mass flowrate is defined as $\tilde{m} = m/m_{scale}$, where the mass flow rate m_{scale} is calculated for the optimal radial configuration ($\alpha_o = 27.3°$ e $\mathrm{Be} = 10^8$). The boundary conditions are shown in Fig. 2. The dimensionless pressure difference Be is defined in accordance with the definition proposed by Bhattacharjee and Grosshandler [17] and Petrescu [18].

Eqs. (5)–(8) were solved by using a CFD package based on tetrahedral volume elements [19,20]. The grid was non-uniform in all directions, and varied from one geometry to the next. The appropriate mesh size was determined by successive refinements, approximately doubling the number of elements from one mesh size to the next mesh size until the criterion $|(\tilde{T}^j_{max} - \tilde{T}^{j+1}_{max})/\tilde{T}^j_{max} < 5 \times 10^{-3}$ was satisfied. Here $\tilde{T}^j_{max}$ represents the maximum temperature calculated using the current mesh, and $\tilde{T}^{j+1}_{max}$ corresponds to the next mesh, in which the number of elements was doubled. The following results were obtained by using between 6×10^5 and 1.2×10^6 tetrahedral volume elements. Table 1 gives an example of how grid independence was achieved. Note that the mesh was much more refined in the fluid region than in the solid region.

The accuracy of these numerical results was tested by solving Eqs. (5) and (8) with our current code, which uses a pressure based solver (coupled/2nd order for pressure/2^{2nd} upwind scheme for momentum and energy) [19], and comparing the results with the results obtained using a segregated solver (Simple/Standard for pressure/1st order upwind scheme for momentum and energy) [20] for the domain shown in Fig. 2. Table 2 shows that the results agree within 1.3%. Convergence was achieved when the following maximal residuals were reached: 10^{-4} for mass and momentum equations and 10^{-8} for energy equation. Double precision was used for all numerical simulations.

Table 1
Numerical tests showing the attainment of grid independence ($\Phi = 0.05$, $y_1 = 0.515$ ($\alpha = 27.3°$), $\mathrm{Be} = 10^8$, $Pr = 0.7$.

Number of elements		$\tilde{T}^j_{max}$	$\lvert(T^j_{max} - T^{j+1}_{max})/T^j_{max}\rvert$
Solid	Fluid		
547,751	138,905	0.5211	2.3×10^{-3}
962,268	283,155	0.5223	

Table 2
Comparison between the results obtained using our code (pressure based solver – coupled – upwind scheme [19]) and segregated solver – simple – upwind scheme [20] ($\Phi = 0.05$, $y_1 = 0.515$ ($\alpha = 27.3°$), $\mathrm{Be} = 10^8$, $Pr = 0.7$.

Pressure based solver $\tilde{T}_{max}$	Segregated solver $\tilde{T}_{max}$
0.5211	0.5277

3. Radial channels

Fig. 3 shows the minimization of the maximum temperature $\tilde{T}_{max}$ with respect to the length $\tilde{y}_1$ for several values of the volume fraction ϕ. We used $\mathrm{Be} = 10^8$, $Pr = 0.7$, $\tilde{k} = 0.9$, $\tilde{C} = 1.2$ and $\tilde{\rho} = 55.3$. The optimal values ($\tilde{y}_{1,o}$,$\tilde{T}_{max,m}$) discovered in Fig. 3 are summarized in Fig. 4. The minimal maximum temperature decreases when the value of the volume fraction ϕ increases. The optimal angle α and length $\tilde{y}_1$ are relatively insensitive to changes in ϕ .

Fig. 5 shows the temperature distribution on the top and bottom surfaces of the square slab, in the best flow configurations

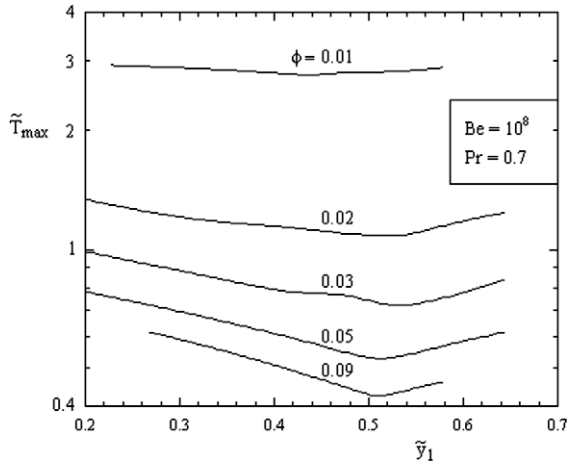

Fig. 3. The minimization of the maximum temperature with respect to $\tilde{y}_1$.

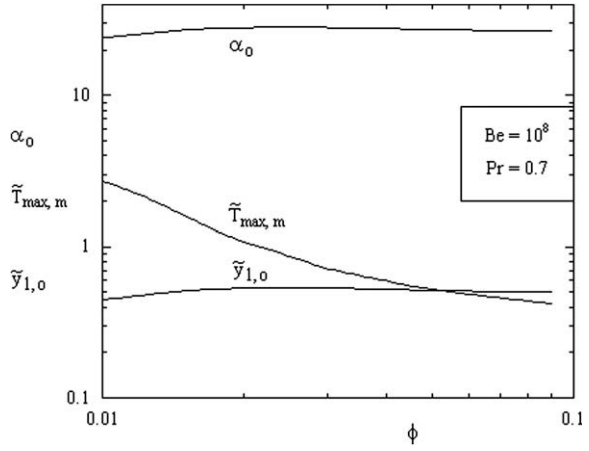

Fig. 4. The optimized geometry and performance as functions of volume fraction.

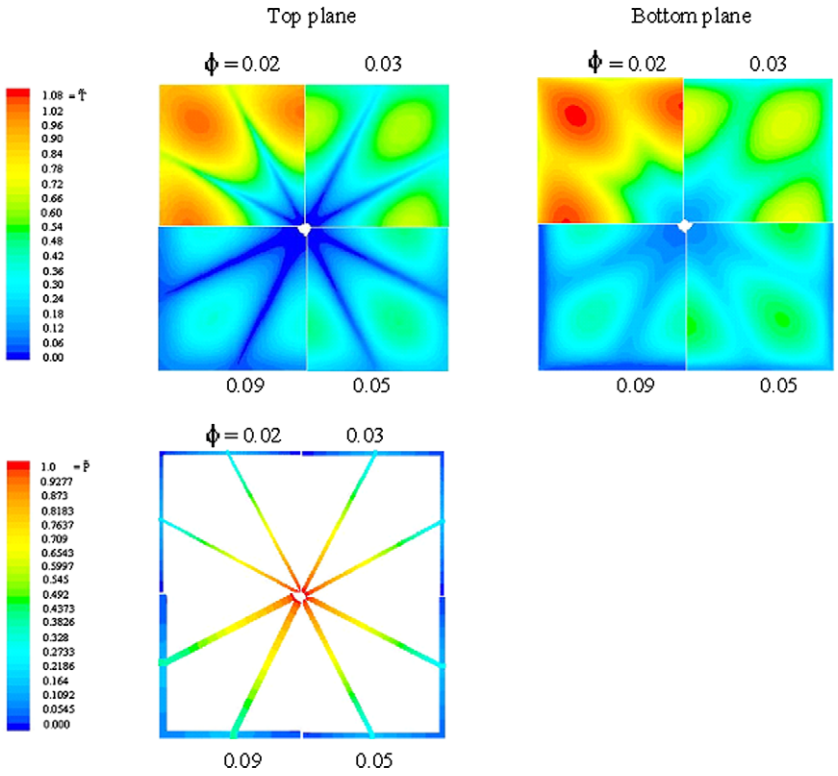

Fig. 5. The temperature distribution on the top and bottom surfaces, and the pressure field on the top surface of the channels for the optimized radial design.

determined in Fig. 4. If each square slab is divided into four parts, the top-left shows the results for $\phi = 0.02$, the top-right $\phi = 0.03$, the bottom-right $\phi = 0.05$ and the bottom-left $\phi = 0.09$. The maximal temperatures occur on the bottom surface of the body (see the red spots[1] in Fig. 5), and their positions vary depending on the angle α. Fig. 5 (bottom) shows the pressure distribution field on the top surface of the channels corresponding to the same volume fractions as in Fig. 5.

4. Dendritic design with one level bifurcation

Consider next the design with Y-shaped channels shown in Fig. 6. The structure is similar to Fig. 2, except that the duct bifurcates into two branches that form the angle β. The volume occupied by the ducts is

$$V_p = V_a + V_b + V_c + V_d + V_e \tag{11}$$

where

$$V_a = L_0 D_0^2 \tag{12}$$

$$V_b = (L_1 + t - D_1) D_1^2 \tag{13}$$

$$V_c = (L_2 + t - D_2) D_2^2 \tag{14}$$

$$V_d = y_1 D_2^2 + (y_3 - D_1) D_1^2 + (L - y_1 - y_3 - D_1 - D_2)(D_1^2 + D_2^2)/2 \tag{15}$$

$$V_e = \frac{1}{2} D_1^3 \tag{16}$$

The resulting structure has more degrees of freedom than in Fig. 2. To begin with, the channel size ratios D_0/D_1 and D_0/D_2 vary, but their optimal values are not the same as those recommended by the Hess–Murray rule ($D_0/D_1 = D_0/D_2 = 2^{1/3}$). It was shown that

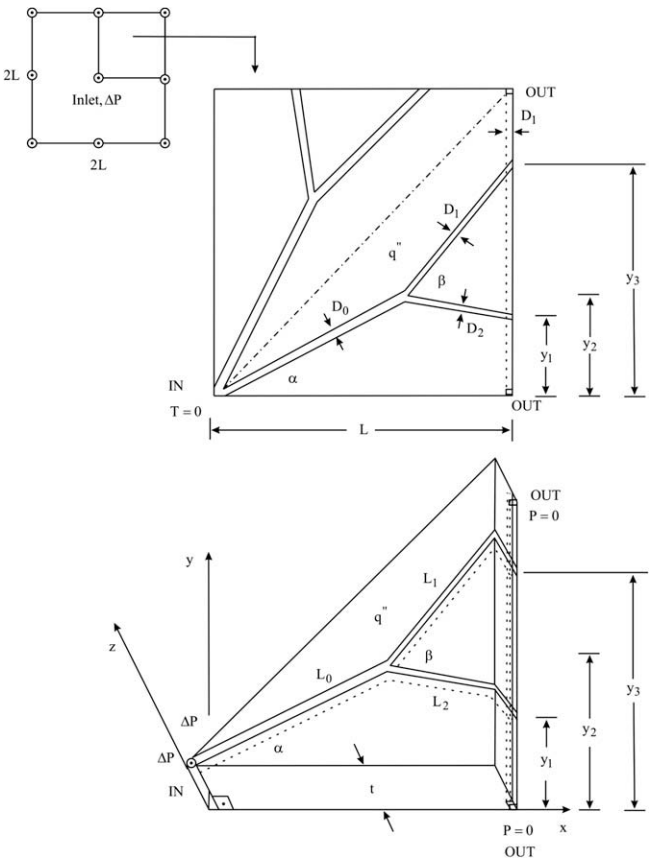

Fig. 6. Design with channels with one level of bifurcation.

[1] For interpretation of the references to color in this figure legend, the reader is referred to the web version of this paper.

the Hess–Murray rule is valid only when the Y-shaped construct has two identical branches ($L_1 = L_2$, $D_1 = D_2$), and that in general the optimized D ratios depend on L ratios as follows [21]:

$$\frac{D_0}{D_1} = \left[1 + \left(\frac{L_2}{L_1}\right)^3\right]^{1/3} \tag{17}$$

$$\frac{D_0}{D_2} = \left[1 + \left(\frac{L_1}{L_2}\right)^3\right]^{1/3} \tag{18}$$

Because of Eqs. (17) and (18), the design of Fig. 6 is left with only three degrees of freedom, namely y_1, L_0 and y_2 (or α). Note also that $y_3 = L - y_1$.

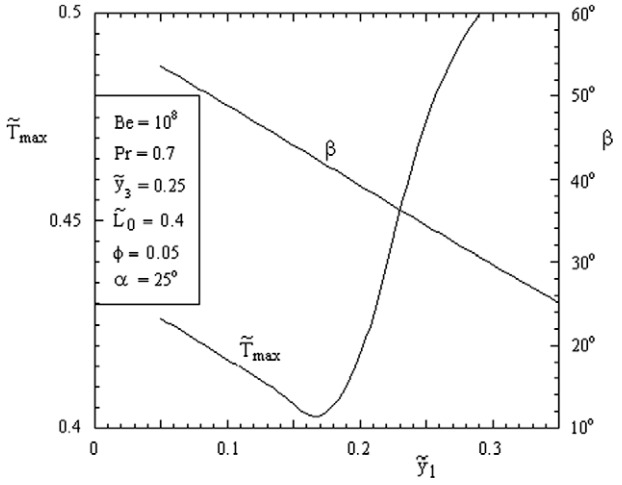

Fig. 7. The minimization of the hot-spot temperature with respect $\tilde{y}_1$, in the design with one level of bifurcation.

We optimized the dendritic design of Fig. 6 in the same way as the radial design of Fig. 2. We searched for the configuration with minimum $\tilde{T}_{max}$, regardless of the locations of the spots with $\tilde{T}_{max}$. When the configuration with "optimal distribution of imperfection" [2] is found, the hot spots (shown in red in Figs. 5 and 8) should have the same intensity, and, in addition, their color is the least red. In such configurations, $\tilde{T}_{max}$ is labeled $\tilde{T}_{max,m}$, no matter where $\tilde{T}_{max,m}$ occurs. Fig. 7 shows that there is a minimal $\tilde{T}_{max}$ when the length $\tilde{y}_1$ varies and the other geometrical parameters ($\tilde{y}_3, \tilde{L}_0, \alpha$) are fixed. The optimal angle β decreases linearly when $\tilde{y}_1$ increases. Fig. 8 shows the temperature distribution on the top and bottom surfaces of the configuration of Fig. 6, which was optimized in Fig. 7. The pressure field in the top plane of the channels of the optimal geometry (Fig. 7) is shown in the lower part of Fig. 8.

Fig. 9 shows the behavior of the hot-spot temperature for several values of $\tilde{L}_0$. The minimum of the $\tilde{T}_{max}$ ($\tilde{y}_1$)envelope represents a second opportunity for optimization. The optimal configurations determined this manner are summarized in Fig. 10, where the minimal maximum temperature $\tilde{T}_{max,m}$ is reported as a function of $\tilde{L}_0$. The corresponding optimal angle β_o is proportional to $\tilde{L}_0$

In Fig. 10, we see that the minimum of the $\tilde{T}_{max,m}(\tilde{L}_0)$ curve occurs at $\tilde{L}_0 \cong 0.44$. This minimum is relatively shallow. On the vertical line $\tilde{L}_0 = 0.44$ we read the other geometrical features of the Y-shaped configuration: $\beta_0 = 44.8°$ and $\tilde{y}_{1,0} = 0.17$. These features correspond to the assumed $\tilde{y}_3 = 0.25$ and $\alpha = 25°$. This optimal configuration is sketched in Fig. 10.

5. Dendritic design with two levels of bifurcation

The design with two levels of bifurcation is shown in Fig. 11. The structure is similar to Fig. 6, except that the two branches that form the angle β now bifurcate into branches that form the angles γ and δ. The volume occupied by the ducts is $V_p = V_a + V_b + V_c + V_d + V_e$, where

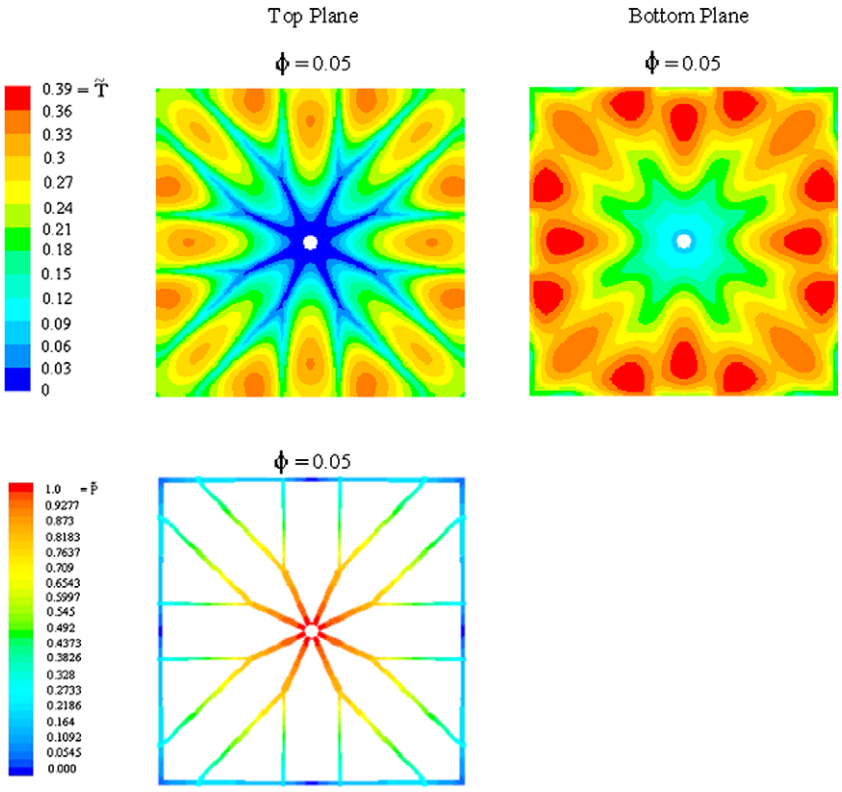

Fig. 8. The temperature distribution on the top and bottom body surfaces, and the pressure field on the top surface of the channels for the optimal design of Fig. 7.

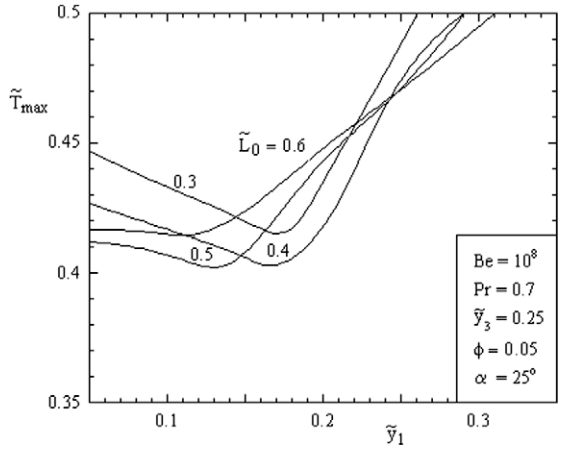

Fig. 9. The effect of $\tilde{L}_0$ and $\tilde{y}_1$ on the hot-spot temperature in the design with one level of bifurcation.

$$V_a = \sum_{i=0}^{6} L_i D_i^2 \tag{19}$$

$$V_b = (t + y_1 + h_1/2)D_4^2 \tag{20}$$

$$V_c = [t + (h_1 + h_2)/2]D_3^2 \tag{21}$$

$$V_d = [t + (h_2 + h3)/2]D_6^2 \tag{22}$$

$$V_e = (t + h_3/2 + h_4 + 0.5D_s)D_5^2 \tag{23}$$

The lengths t, h_i, L_i and D_i, that appear in these equations are shown in Fig. 11. The optimal ratios between diameters are given by Eqs. (17) and (18) and

$$\frac{D_1}{D_5} = \left[1 + \left(\frac{L_6}{L_5}\right)^3\right]^{1/3}, \quad \frac{D_1}{D_6} = \left[1 + \left(\frac{L_5}{L_6}\right)^3\right]^{1/3} \tag{24}$$

$$\frac{D_2}{D_3} = \left[1 + \left(\frac{L_4}{L_3}\right)^3\right]^{1/3}, \quad \frac{D_2}{D_4} = \left[1 + \left(\frac{L_3}{L_4}\right)^3\right]^{1/3} \tag{25}$$

Eqs. (1), (2), (4), (17)–(25) and the degrees of freedom α, $\tilde{y}_1$, L_0, L_1/L_0, L_2/L_0, L_3/L_0, L_4/L_0, L_5/L_0 and L_6/L_0 are the information needed to calculate the flow in each geometry with two levels of bifurcation.

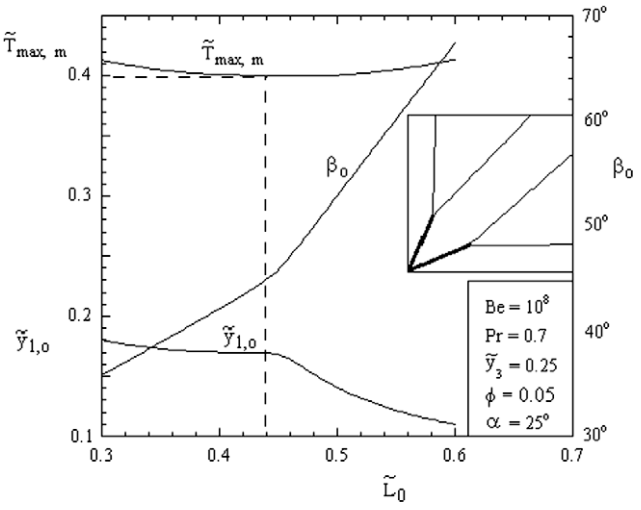

Fig. 10. The minimization of the hot-spot temperature with respect to $\tilde{L}_0$ in the design with one level of bifurcation.

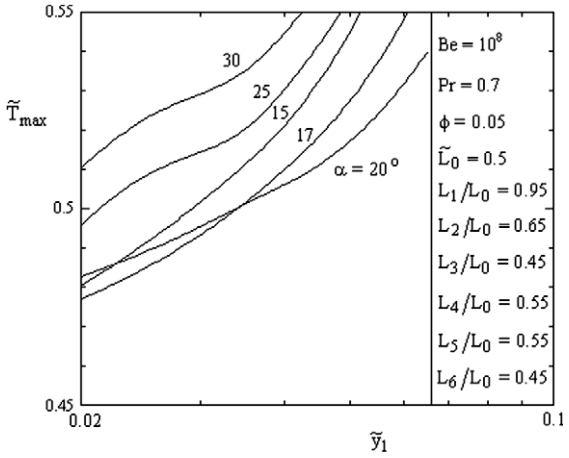

Fig. 12. The effect of α and $\tilde{y}_1$ on the hot-spot temperature in the design with two levels of bifurcation.

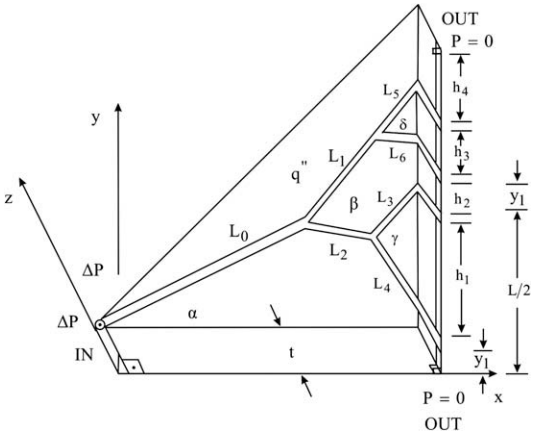

Fig. 11. Dendritic design with two levels of bifurcation.

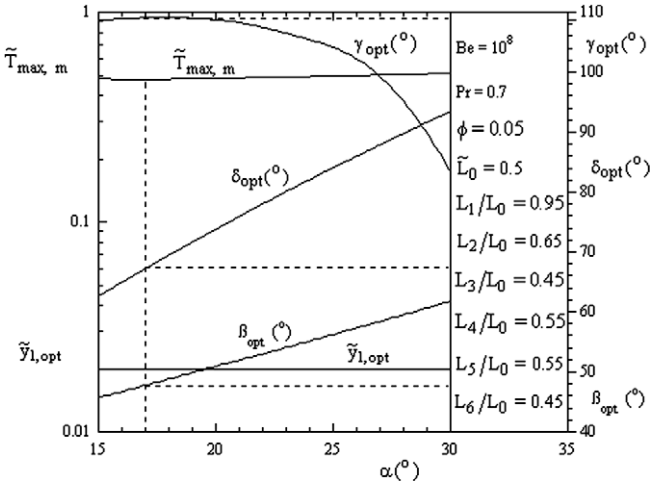

Fig. 13. The twice minimized hot-spot temperature in the design with two levels of bifurcation.

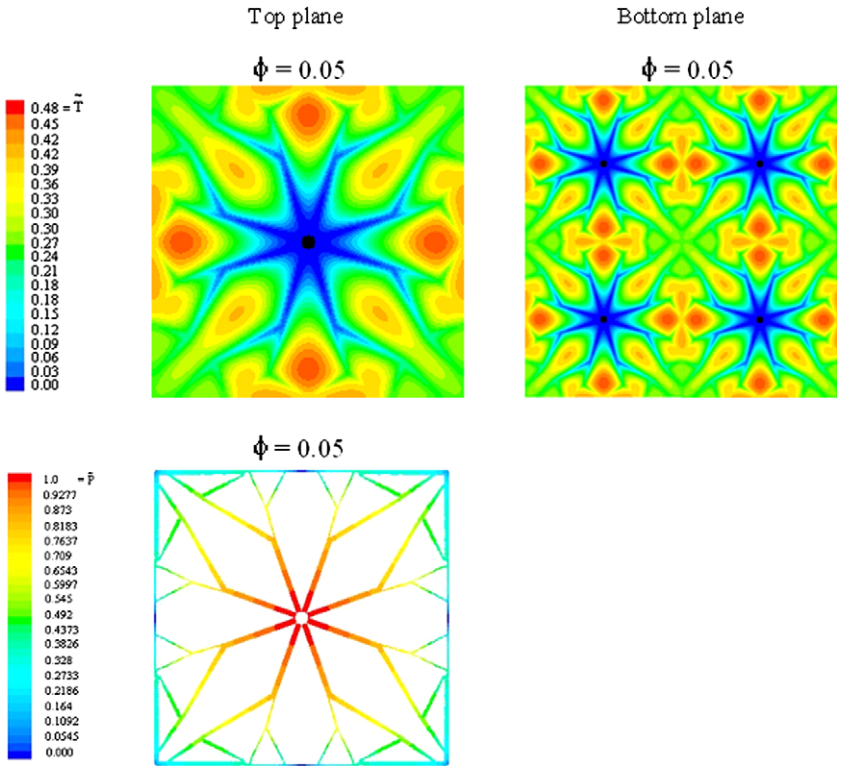

Fig. 14. The temperature distribution on the top and bottom surfaces and the pressure field on the top surface of the channels for the optimal design of the type shown in Fig. 13.

Fig. 12 shows the effect of the angle α and the length $\tilde{y}_1$ on the maximal temperature. This figure shows that $\tilde{T}_{max}$ decreases when the length $\tilde{y}_1$ decreases. The best length is $\tilde{y}_{1,opt} = 0.02$, for all the studied angles α.

These results are summarized in Fig. 13, where the optimal angles for each bifurcation are also shown. The optimal geometry that can be obtained using the set of constraints presented in this figure is $\alpha_o = 17°$, $y_{1,oo} = 0.02$, $\beta_{oo} = 48°$, $\delta_{oo} = 67°$ and $\gamma_{oo} = 109°$. The corresponding minimized maximal temperature is $\tilde{T}_{max,mm} = 0.477$. The subscript "o" means that one parameter (the angle) was optimized once while the subscripts "oo" and "mm" mean that the parameters were optimized twice. The top and bottom views of the temperature distribution calculated for this optimal structure are shown in the upper part of Fig. 14. This figure shows that the vascularized configuration depresses the highest temperature by 8.5% relative to the optimal radial configuration, and also improves the distribution of the hot spots. The lower part of Fig. 14 also shows the pressure field on the top surface of the channels of this optimal configuration.

6. Dendritic design with three levels of bifurcation

The main features of the design with three levels of bifurcation are shown in Fig. 15. The volume occupied by the ducts is $\tilde{V}_p = \tilde{V}_a + \tilde{V}_b + \tilde{V}_c + \tilde{V}_d + \tilde{V}_e + \tilde{V}_f + \tilde{V}_g$, where

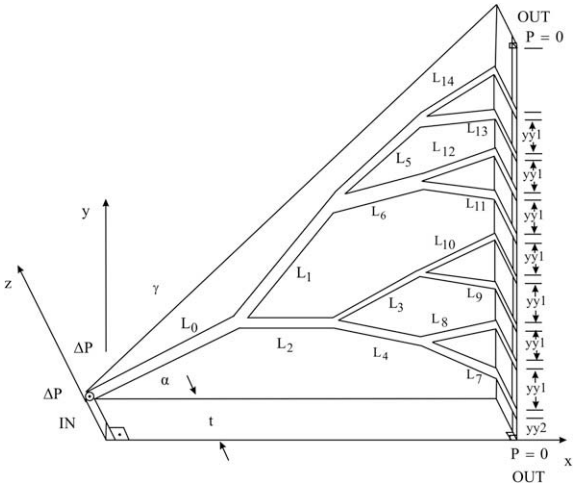

Fig. 15. Dendritic design with three levels of bifurcation.

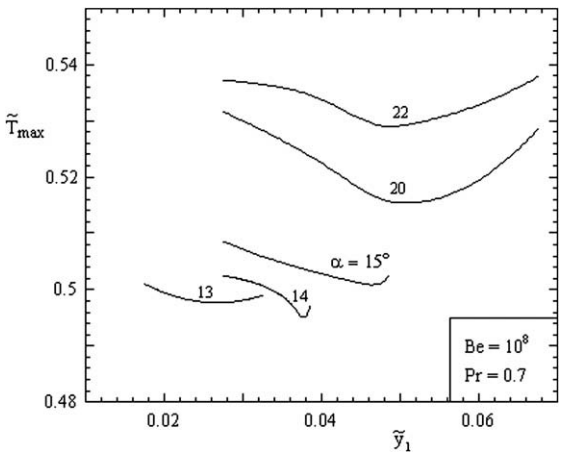

Fig. 16. The effect of $\tilde{y}_1$ and α on the hot-spot temperature in the design with three levels of bifurcation.

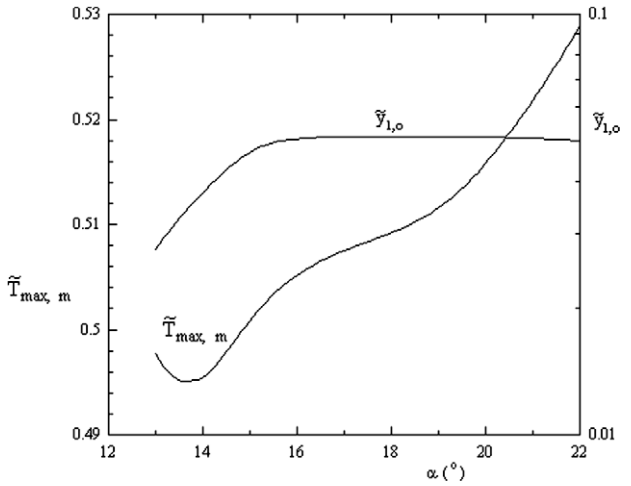

Fig. 17. The minimization of the hot-spot temperature with respect to α in the design with three levels of bifurcation.

$$\tilde{V}_a = \sum_{i=0}^{14} \tilde{L}_i \tilde{D}_1^2, \quad \tilde{V}_d = (\tilde{D}_{14}^3)/2 \tag{26}$$

$$\tilde{V}_b = \sum_{i=7}^{14} 2\tilde{D}_i^3, \quad \tilde{V}_e = \sum_{i=7}^{13} \widetilde{yy1}(\tilde{D}_i^2 + \tilde{D}_{i+1}^2)/2 \tag{27}$$

$$\tilde{V}_c = \sum_{i=7}^{14} (t - 2\tilde{D}_i)\tilde{D}_i^2, \quad \tilde{V}_f = \widetilde{y1}(\tilde{D}_7^2 + \tilde{D}_8^2)/2 \tag{28}$$

$$\tilde{V}_g = (2\widetilde{yy1} - \widetilde{y1})(\tilde{D}_{13}^2 + \tilde{D}_{14}^2)/2 \tag{29}$$

Note that the length $\widetilde{yy1}$ is calculated by using

$$\widetilde{yy1} = (1 - (\tilde{D}_7 + \tilde{D}_8 + \tilde{D}_8/2 + \tilde{D}_9 + \tilde{D}_{10} + \tilde{D}_{11} + \tilde{D}_{12} + \tilde{D}_{14} + 2\tilde{D}_{13}))/9 \tag{30}$$

because it is the y distance between two adjacent ports in the plane $x = L$. Note that $\widetilde{y1}$ is a new degree of freedom in the morphing of the flow configuration. Again the relationships between diameter ratios and length ratios are given by Eqs. (17), (18), (24) and (25) and the following equations

$$\frac{\tilde{D}_3}{\tilde{D}_9} = \left[1 + \left(\frac{\tilde{L}_{10}}{\tilde{L}_9}\right)^3\right]^{1/3}, \quad \frac{\tilde{D}_5}{\tilde{D}_{13}} = \left[1 + \left(\frac{\tilde{L}_{14}}{\tilde{L}_{13}}\right)^3\right]^{1/3} \tag{31}$$

$$\frac{\tilde{D}_3}{\tilde{D}_{10}} = \left[1 + \left(\frac{\tilde{L}_9}{\tilde{L}_{10}}\right)^3\right]^{1/3}, \quad \frac{\tilde{D}_5}{\tilde{D}_{14}} = \left[1 + \left(\frac{\tilde{L}_{14}}{\tilde{L}_{13}}\right)^3\right]^{1/3} \tag{32}$$

$$\frac{\tilde{D}_4}{\tilde{D}_8} = \left[1 + \left(\frac{\tilde{L}_7}{\tilde{L}_8}\right)^3\right]^{1/3}, \quad \frac{\tilde{D}_6}{\tilde{D}_{11}} = \left[1 + \left(\frac{\tilde{L}_{12}}{\tilde{L}_{11}}\right)^3\right]^{1/3} \tag{33}$$

$$\frac{\tilde{D}_4}{\tilde{D}_7} = \left[1 + \left(\frac{\tilde{L}_8}{\tilde{L}_7}\right)^3\right]^{1/3}, \quad \frac{\tilde{D}_6}{\tilde{D}_{12}} = \left[1 + \left(\frac{\tilde{L}_{11}}{\tilde{L}_{12}}\right)^3\right]^{1/3} \tag{34}$$

To determine all the dimensions uniquely, it is necessary to solve Eqs. (1), (2), (4), (17)–(33), (34). The degrees of freedom and parameters α, $\tilde{y}_1$, ϕ, $\tilde{t}$, $\tilde{L}_0$ and $\tilde{L}_i/\tilde{L}_0$, i = 1, 14, are the information needed to calculate the geometry for the design with three levels of bifurcation. We fixed the following parameters while optimizing the free variables α and $\tilde{y}_1$: $\phi = 0.5$, $\tilde{t} = 0.1$, $\tilde{L}_0 = 0.5$ $L_1/L_0 = 0.74$, $L_2/L_0 = 0.53$, $L_3/L_0 = 0.25$, $L_4/L_0 = 0.3$, $L_5/L_0 = 0.53$, $L_6/L_0 = 0.47$, $L_7/L_0 = 0.3$, $L_8/L_0 = 0.32$, $L_9/L_0 = 0.26$, $L_{10}/L_0 = 0.27$, $L_{11}/L_0 = 0.27$, $L_{12}/L_0 = 0.28$, $L_{13}/L_0 = 0.28$ and $L_{14}/L_0 = 0.34$. Fig. 16 shows the effect of the length $\tilde{y}_1$ and angle α

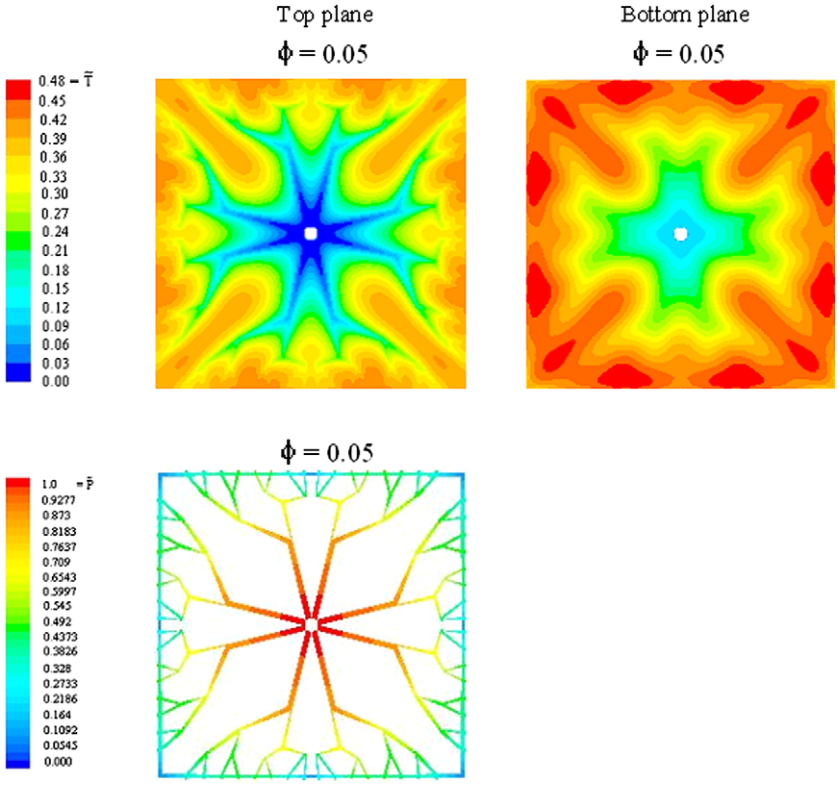

Fig. 18. The temperature distribution on the top and bottom surfaces and the pressure field on the top surface of the channels for the optimal design of the type shown in Fig. 17.

on the maximal temperature: there is an optimal angle for which the hot-spot temperature is minimum.

The results developed in Fig. 16 are summarized in Fig. 17 where $\alpha_o \approx 14°$ and $\widetilde{y}_{1,oo} = 0.038$ emerge as optimal parameters for the design with three levels of bifurcation. The corresponding minimized maximal temperature is $\widetilde{T}_{max,mm} = 0.494$. This configuration performs 5.3% better when compared with the optimal radial configuration, but it is 3.4% inferior relative to the optimal configuration with two levels of bifurcation. The temperature distribution on the top and bottom surfaces and the pressure field on the top surface of the channels for the optimal design obtained in Fig. 17 is shown in Fig. 18.

7. Conclusions

In this paper, we outlined the main steps of the generation of tree-shaped flow architecture for cooling that is imbedded to intercept the intense heat flux that impinges on a wall. The flow architecture is configured as a patchwork of elemental square-shaped slabs, each cooled with a tree-shaped vasculature (Fig. 1). The coolant enters through the center of the element and exits through ports distributed along the square perimeter.

The numerical simulations of heat and fluid flow in three dimensions showed that it is possible to optimize the main features of the tree-shaped configuration. As the complexity of each tree increases from radial channels to three levels of bifurcation, the global thermal resistance of the architecture decreases. The steps of improvement become smaller as the number of bifurcation levels increases. Diminishing returns put an end to the economical search for better flow architectures. This "end" deserves further exploration, because it is here that the merits of the cooling architecture must be properly assessed against the merits of the design with respect to other concerns such as overall pressure drop, and ease of assembly of optimized panels on larger walls, e.g., Figs. 1 and 19.

Fig. 20 shows the behavior of the global thermal resistance as function of the pressure difference maintained across the flow structure. When Be is of order 10^7, the radial designs ($n = 0$) offer lower thermal resistance. When Be is of order 10^8, the dendritic configurations perform better than radial configuration: the best is the $n = 1$ design. At the opposite end of the pressure difference range documented in this study (Be $\sim 10^6$), the dendritic design with one level of bifurcation is again better than the radial design. These conclusions are reinforced by Fig. 21, where on the abscissa we used the

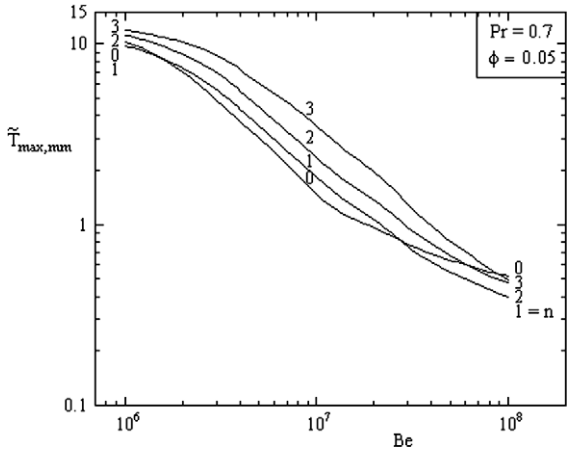

Fig. 20. The behavior of the global thermal resistance versus of the global pressure difference.

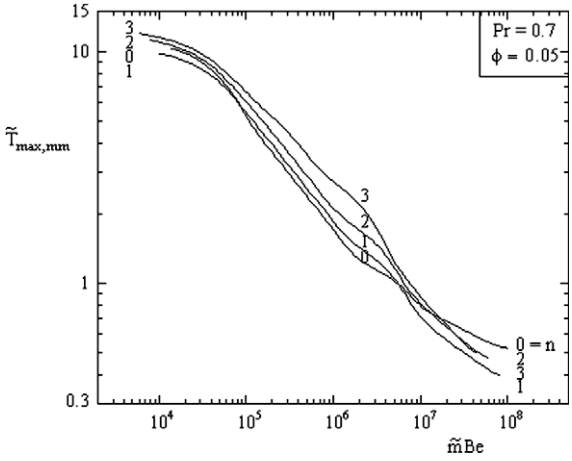

Fig. 21. The behavior of the global thermal resistance versus the pumping power.

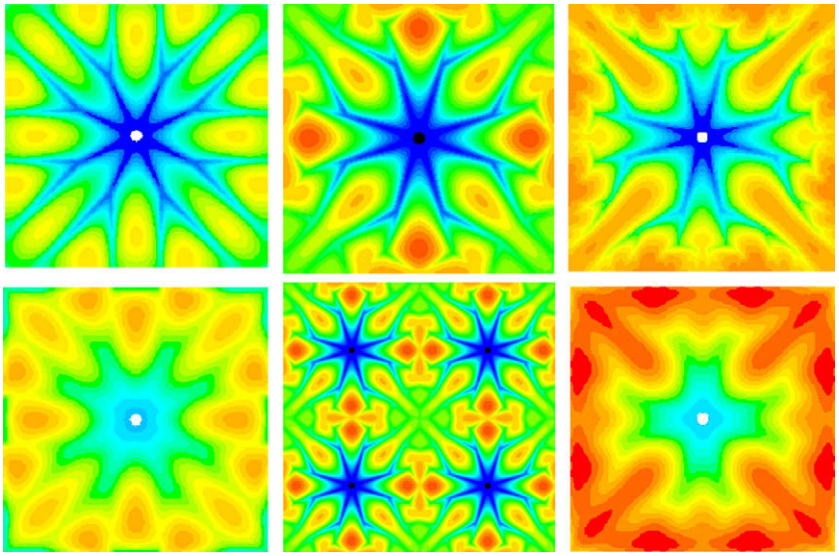

Fig. 19. Larger body cooled with a patchwork of optimized building blocks such as the design proposed in Figs. 1 and 2.

group $\widetilde{m}$Be that is proportional to the pumping power required by the design.

The chief conclusion is that there is not a single architecture that is "best" over the entire range of applications (Be, or $\widetilde{m}$Be). The dendritic designs have their own domain of applicability, and the radial designs have theirs. Important is to know the "transitions" between the winning flow architectures, i.e., when to use which type of design.

Acknowledgement

This work was supported by a grant from the Air Force Office of Scientific Research for "Constructal technology for thermal management of aircraft".

References

[1] A. Bejan, Advanced Engineering Thermodynamics, second ed., Wiley, New York, 1997.
[2] A. Bejan, Shape and Structure from Engineering to nature, Cambridge University Press, Cambridge, UK, 2000.
[3] A.H. Reis, Constructal view of scaling laws of river basins, Geomorphology 78 (2006) 201–206.
[4] A.H. Reis, A.F. Miguel, M. Aydin, Constructal theory of flow architecture of the lungs, J. Med. Phys. 31 (2004) 1135–1140.
[5] A. Bejan, J.H. Marden, Constructing animal locomotion from new thermodynamics theory, Am. Sci. 94 (2006) 342–349.
[6] A.H. Reis, Constructal theory: from engineering to physics and how flow systems develop shape and structure, Appl. Mech. Rev. 59 (2006) 269–282.
[7] S.M. Senn, D. Poulikakos, Tree network channels as fluid distributors constructing double-staircase polymer electrolyte fuel cells, J. Appl. Phys. 96 (2004) 842–852.
[8] X.-Q. Wang, A.S. Mujumdar, C. Yap, Numerical analysis of blockage and optimization of heat transfer performance of fractal-like microchannel nets, J. Electron. Packaging 128 (2006) 38–45.
[9] V.A.P. Raja, T. Basak, S.K. Das, Heat transfer and fluid flow in a constructal heat exchanger, in: R.K. Shah, M. Ishizuka, T.M. Rudy, V.V. Wadekar (Eds.), Proceedings of the Fifth International Conference on Enhanced, Compact and Ultra-Compact Heat Exchangers: Science, Engineering and Technology, Engineering Conferences International, Hoboken, NJ, September 2005.
[10] F. Lundell, B. Thonon, J.A. Gruss, Constructal networks for efficient cooling/heating, in: Second Conference on Microchannels and Minichannels, Rochester, NY, 2004.
[11] Y.S. Muzychka, Constructal design of forced convection cooled microchannel heat sinks and heat exchangers, Int. J. Heat Mass Transfer 48 (2005) 3119–3127.
[12] N. Kockmann, T. Kiefer, M. Engler, P. Woias, Channel networks for optimal heat transfer and high throughput mixers, in: ECI International Conference on Heat Transfer and Fluid Flow in Microscale, Castelvecchio Pascoli, Italy, September 2005.
[13] A. Bejan, S. Lorente, K.-M. Wang, Networks of channels for self-healing composite materials, J. Appl. Phys. 100 (2006) 033528.
[14] S. Kim, S. Lorente, A. Bejan, Vascularized materials: tree-shaped flow architectures matched canopy to canopy, J. Appl. Phys. 100 (2006) 063525.
[15] S. Lorente, A. Bejan, Svelteness, freedom to morph and constructal multi-scale flow structures, Int. J. Therm. Sci. 44 (2005) 1123–1130.
[16] A. Bejan, S. Lorente, Constructal theory of generation of configuration in nature and engineering, J. Appl. Phys. 100 (2006) 041301.
[17] S. Bhattachajee, W.L. Grosshandler, The formation of wall jet near a high temperature wall under microgravity environment, ASME HTD 96 (1988) 711–716.
[18] S. Petrescu, Comments on the optimal spacing of parallel plates cooled by forced convection, Int. J. Heat Mass Transfer 37 (1994) 1283.
[19] Fluent (version 6.3.16), ANSYS, Inc., 2007.
[20] Fluent (version 6.2.16), ANSYS, Inc., 2005.
[21] A. Bejan, S. Lorente, Design with Constructal Theory, Wiley, Hoboken, 2008. Problem 4.4.